Available online at www.sciencedirect.com
SCIENCE DIRECT®
ELSEVIER
International Journal of Solids and Structures 42 (2005) 6550–6565
INTERNATIONAL JOURNAL OF SOLIDS and STRUCTURES
www.elsevier.com/locate/ijsolstr

An application of a damage constitutive model to concrete at high temperature and prediction of spalling

Rosen Tenchev *, Phil Purnell

Department of Civil Engineering, University of Warwick, CV4 7AL, UK

Received 25 May 2004; received in revised form 5 June 2005
Available online 20 July 2005

Abstract

A characteristic feature of concrete under uniaxial compression is the development of cracks parallel to the loading direction. A damage constitutive model proposed by Ortiz [Ortiz, M., 1985. A constitutive theory for the inelastic behaviour of concrete. Mech. Mater. 4, 67–93] can predict the transverse tensile stress responsible for these cracks by considering the interaction between the aggregate and the mortar and the development of damage in the latter. When concrete is exposed to high temperature, as is the case during fire, the failure mode is thermal spalling. In order to improve the prediction of the stresses involved in this failure Ortiz's model is extended to account for the effects of high temperature. Published experimental results for uniaxial and biaxial compression at high temperatures are used to calibrate the temperature dependence of some of the material properties. The transient creep strain is accounted for by modifying the constrained thermal strain. The stress analysis is coupled with hygro-thermal analysis of heat, mass transfer and pore pressure build-up. The effect of pore pressure on the damage evolution is modeled by applying a body force in the stress analysis module proportional to the pressure gradient. A numerical example of concrete under fire is solved and the computed results are discussed. Spalling is predicted when the damage variable reaches its maximum value of unity. The predicted depth and time of spalling for a range of variation of permeability and initial liquid water content are presented. They are in good agreement with published experimental results.

Keywords: Material model; Thermal stress; Pore pressure; Damage; Spalling

1. Introduction

Various material models for concrete at high temperature have been proposed based on plasticity, damage, or a combination between them.

* Corresponding author. Tel.: +44 121 475 0954; fax: +44 247 641 8922.
E-mail address: R.Tenchev@warwick.ac.uk (R. Tenchev).

0020-7683/$ - see front matter © 2005 Elsevier Ltd. All rights reserved.
doi:10.1016/j.ijsolstr.2005.06.016

Simo and Ju (1987), employing irreversible thermodynamics and an internal state variable, developed continuous elasto-plastic damage models within two alternative dual frameworks—strain based and stress based. Carol et al. (1994) presented a unified theory of elastic degradation and damage based on a loading surface. Papa and Taliecio (1996) used two second-order damage tensors describing the surface damage induced by the tensile and compressive strains, and a scalar variable describing the volumetric damage in their anisotropic damage model. Faria et al. (1998) proposed a strain-based plastic viscous model for massive concrete structures. Ulm et al. (1999) used a thermo–chemo-plastic constitutive equation to compute the thermal damage, decohesion, stresses and spalling in the numerical analysis of the 1996 fire in the Channel Tunnel. Nechnech et al. (2002) and Luccioni et al. (2003) used an elasto-plastic damage model in which the thermal damage was defined via the variation of the elastic modulus with temperature.

Baggio et al. (1995) presented thermo–hydro-mechanical analysis of concrete, which was later coupled with damage at high temperature in Gawin et al. (1999). In these two publications the whole complexity of modeling concrete at high temperature was very well described.

A shortcoming of all of the above methods is that they do not explain the development of cracks parallel to the uniaxial compressive load. Such cracks are observed to appear even if there is slight lateral constraining pressure, although fracture mechanics does not allow cracks to open under compressive loading. The contradiction is overcome in the material model proposed by Ortiz (1985), which considers concrete as a mixture of aggregate and mortar. Tensile transverse stress can be predicted under compressive loading as a result of the interaction between aggregate and mortar and the development of damage in the latter. The model is further developed by Yazdani and Schreyer (1998) who postulate a more complicated and realistic kinetic theory for the compressive mode of cracking.

When concrete is exposed to high temperature, as is the case during fire, the failure mode is thermal spalling. It is often explosive in manner and very dangerous for the integrity of the concrete structure. Spalling is the result of the combined effect of stresses (mechanical and thermal) and pore pressure. The planes of spalling are usually parallel to the main compressive stress. The transverse tensile stress in the mortar, as predicted by Ortiz's model, may have a significant effect on this type of failure.

In the present paper the model proposed by Ortiz (1985) is further developed to account for the effect of high temperature and the temperature dependence of the material properties. The model is incorporated in a finite element coupled hygro–thermo-stress analysis program developed by the authors and is used for the prediction of thermal spalling.

2. Formulation of the constitutive model

Concrete is treated as a two-phase material consisting of mortar and coarse aggregate with volume fractions α_1 and α_2, respectively, and $\alpha_1 + \alpha_2 = 1$. According to the mixture theory used (Ortiz, 1985), there is displacement compatibility between the phases ($\boldsymbol{\varepsilon} = \boldsymbol{\varepsilon}_1 = \boldsymbol{\varepsilon}_2$) and the phase stresses jointly equilibrate the external stresses ($\boldsymbol{\sigma} = \alpha_1\boldsymbol{\sigma}_1 + \alpha_2\boldsymbol{\sigma}_2$). Here $\boldsymbol{\varepsilon}$ and $\boldsymbol{\sigma}$ denotes the strain and stress tensor. Subscript '1' is used for quantities pertinent to the mortar, subscript '2' for those pertinent to the aggregate. The stress $\boldsymbol{\sigma}_2$ may be considered as a tensor representing the contact forces, which are acting among aggregate particles and surrounding mortar. In rate form

$$\dot{\boldsymbol{\varepsilon}} = \dot{\boldsymbol{\varepsilon}}_1 = \dot{\boldsymbol{\varepsilon}}_2 \tag{1}$$

$$\dot{\boldsymbol{\sigma}} = \alpha_1\dot{\boldsymbol{\sigma}}_1 + \alpha_2\dot{\boldsymbol{\sigma}}_2 \tag{2}$$

The incremental stress–strain relationship is $\dot{\boldsymbol{\sigma}} = \mathbf{D}^{(T)}\dot{\boldsymbol{\varepsilon}}$. The tangent stiffness of concrete is

$$\mathbf{D}^{(T)} = \alpha_1\mathbf{D}_1^{(T)} + \alpha_2\mathbf{D}_2^{(T)} \tag{3}$$

where $\mathbf{D}_1^{(T)}$ and $\mathbf{D}_2^{(T)}$ are the tangent stiffness of mortar and aggregate, respectively.

With an increase of temperature, the volume fractions change: mortar shrinks due to dehydration and aggregate expands. In the present analysis they are assumed to be constant. Temperature dependent values may be used in Eqs. (2) and (3) during the incremental numerical analysis, but it has to be noted that it would be still an approximation, because Eq. (2) should read $\dot{\boldsymbol{\sigma}} = \alpha_1(T)\dot{\boldsymbol{\sigma}}_1 + \alpha_2(T)\dot{\boldsymbol{\sigma}}_2 + \dot{\alpha}_1(T)\boldsymbol{\sigma}_1 + \dot{\alpha}_2(T)\boldsymbol{\sigma}_2$, which means that an assumption $\dot{\alpha}_1 = \dot{\alpha}_2 = 0$ has been made.

2.1. Mortar material model

The constitutive model proposed by Ortiz (1985), based on a continuous damage evolution in the compliance tensor, is used. In the present study it is enhanced by taking into account the thermal strain $\boldsymbol{\varepsilon}_{\text{th}}$ and the temperature dependence of the strength and the modulus of elasticity of the mortar.

The stress–strain relationship $\boldsymbol{\varepsilon}_1 = \mathbf{C}_1{:}\boldsymbol{\sigma}_1 + \boldsymbol{\varepsilon}_{\text{th}}$ in rate form is

$$\dot{\boldsymbol{\varepsilon}}_1 = \mathbf{C}_1 : \dot{\boldsymbol{\sigma}}_1 + \dot{\mathbf{C}}_1 : \boldsymbol{\sigma}_1 + \dot{\boldsymbol{\varepsilon}}_{\text{th}} \tag{4}$$

An additive decomposition of the mortar compliance tensors can be assumed

$$\mathbf{C}_1 = \mathbf{C}_1^0 + \mathbf{C}_1^{\text{c}} \tag{5}$$

where $\mathbf{C}_1^0$ is the elastic compliance tensor and $\mathbf{C}_1^{\text{c}}$ is the compliance tensor due to microcracks.

The microcracks are assumed to follow a tortuous path and to be capable of becoming active in two possible modes: mode I, when acted upon by tensile stress normal to their average path, and mode II, when acted upon by compressive stress parallel to their average path. An additive decomposition of $\mathbf{C}_1^{\text{c}}$ can be assumed

$$\mathbf{C}_1^{\text{c}} = \mathbf{P}_1^+ : \bar{\mathbf{C}}_{\text{I}}^{\text{c}} : \mathbf{P}_1^+ + \mathbf{P}_1^- : \bar{\mathbf{C}}_{\text{II}}^{\text{c}} : \mathbf{P}_1^- \tag{6}$$

where $\mathbf{P}_1^+$ and $\mathbf{P}_1^-$ are projection operators

$$\mathbf{P}^+ = \sum_{i=1}^{3} \mathbf{m}_i^+ \otimes \mathbf{m}_i^+ \quad \mathbf{P}^- = \sum_{i=1}^{3} \mathbf{m}_i^- \otimes \mathbf{m}_i^- \tag{7}$$

which are defined via a spectral decomposition of the stress tensor

$$\boldsymbol{\sigma}_1 = \boldsymbol{\sigma}_1^+ + \boldsymbol{\sigma}_1^- = \sum_{i=1}^{3} \hat{\sigma}_i \mathbf{m}_i^+ + \sum_{i=1}^{3} \hat{\sigma}_i \mathbf{m}_i^- \tag{8}$$

where $\boldsymbol{\sigma}_1^+$ and $\boldsymbol{\sigma}_1^-$ are the positive and negative eigenvalues, respectively, and $\mathbf{m}_i^+$ and $\mathbf{m}_i^-$ are the corresponding eigenvalue basis

$$\mathbf{m}_i^+ = \begin{cases} \mathbf{m}_i & \text{if } \sigma_i > 0 \\ \mathbf{0} & \text{if } \sigma_i \leqslant 0 \end{cases}; \quad \mathbf{m}_i^- = \begin{cases} \mathbf{m}_i & \text{if } \sigma_i < 0 \\ \mathbf{0} & \text{if } \sigma_i \geqslant 0 \end{cases} \tag{9}$$

$$\mathbf{m}_1 = \frac{(\boldsymbol{\sigma} - \hat{\sigma}_2\mathbf{1})(\boldsymbol{\sigma} - \hat{\sigma}_3\mathbf{1})}{(\hat{\sigma}_1 - \hat{\sigma}_2)(\hat{\sigma}_1 - \hat{\sigma}_3)}; \quad \mathbf{m}_2 = \frac{(\boldsymbol{\sigma} - \hat{\sigma}_1\mathbf{1})(\boldsymbol{\sigma} - \hat{\sigma}_3\mathbf{1})}{(\hat{\sigma}_2 - \hat{\sigma}_1)(\hat{\sigma}_2 - \hat{\sigma}_3)}; \quad \mathbf{m}_3 = \frac{(\boldsymbol{\sigma} - \hat{\sigma}_2\mathbf{1})(\boldsymbol{\sigma} - \hat{\sigma}_1\mathbf{1})}{(\hat{\sigma}_3 - \hat{\sigma}_1)(\hat{\sigma}_3 - \hat{\sigma}_2)} \tag{10}$$

The flexibility tensors due to microcracks in modes I and II, $\bar{\mathbf{C}}_{\text{I}}^{\text{c}}$ and $\bar{\mathbf{C}}_{\text{II}}^{\text{c}}$ respectively, are defined in a rate form as

$$\dot{\bar{\mathbf{C}}}_{\text{I}}^{\text{c}} = (1-\lambda)\dot{\mu}\frac{\boldsymbol{\sigma}_1^+ \otimes \boldsymbol{\sigma}_1^+}{\boldsymbol{\sigma}_1^+ : \boldsymbol{\sigma}_1^+} \quad \dot{\bar{\mathbf{C}}}_{\text{II}}^{\text{c}} = (1-\lambda)\dot{\mu}c\frac{\boldsymbol{\sigma}_1^- \otimes \boldsymbol{\sigma}_1^-}{\boldsymbol{\sigma}_1^- : \boldsymbol{\sigma}_1^-} \tag{11}$$

where μ is a scalar parameter representing the cumulative irreversible damage ($\dot{\mu} \geqslant 0$); c is a cross-effect coefficient which governs the extent of mode II damage and can be related to the ratio of the tensile and

compressive strengths, $c = (f_t/f_c)^2$; λ is material constant with the help of which a simple model of plastic microcracking can be achieved (purely brittle $\lambda = 0$, to perfectly ductile $\lambda = 1$).

The term involving the rate of the compliance tensor in Eq. (4) is

$$\dot{\mathbf{C}}_1 : \boldsymbol{\sigma}_1 = \dot{\mu}_1 \mathbf{s}_1 + \dot{T} \frac{\partial \mathbf{C}_1}{\partial T} : \boldsymbol{\sigma}_1 \tag{12}$$

where the first term is due to the accumulating damage and $\mathbf{s}_1 = \boldsymbol{\sigma}_1^+ + c\boldsymbol{\sigma}_1^-$, (Ortiz, 1985). The second term is due to the temperature dependence of the modulus of elasticity.

The damage surface is defined as:

$$\Phi_1 = \frac{1}{2}\left[\boldsymbol{\sigma}_1^+ : \boldsymbol{\sigma}_1^+ + c\boldsymbol{\sigma}_1^- : \boldsymbol{\sigma}_1^- - t_1^2(\mu)\right] = 0 \tag{13}$$

where $t_1(\mu)$ plays the role of a critical stress. It can be derived from the uniaxial tensile stress–strain curve. The one proposed by Smith and Young (1955), is used

$$\sigma = \frac{f_t}{\varepsilon_t}\varepsilon \exp\left(1 - \frac{\varepsilon}{\varepsilon_t}\right) = E_0 \varepsilon \exp\left(-\frac{\varepsilon}{\varepsilon_t}\right) = \frac{E_0 \varepsilon}{\exp\left(\frac{\varepsilon}{\varepsilon_t}\right)} \tag{14}$$

where the initial Young's modulus is computed from

$$E_0 = \left(\frac{\partial \sigma(\varepsilon)}{\partial \varepsilon}\right)_{\varepsilon = 0} = \frac{f_t}{\varepsilon_t} e \tag{15}$$

where $e \approx 2.7183$. Ortiz's (1985) damage model in uniaxial state of stress and strain is

$$\sigma = \frac{\varepsilon}{\frac{1}{E_0} + \mu} \tag{16}$$

From Eqs. (14) and (16) it follows that $\varepsilon/\varepsilon_t = \ln(1 + \mu E_0)$ and the uniaxial 'critical stress' is

$$t_1(\mu) \equiv \sigma = f_t \exp\left[\frac{\ln\left(1 + E_1^0 \mu\right)}{1 + E_1^0 \mu}\right] \tag{17}$$

where E_1^0 is the Young's modulus of uncracked mortar, f_t is the tensile strength, ε_t the corresponding strain to f_t. In Eq. (17) $t_1(\mu)$ can be regarded as the stress that will produce damage μ. The latter can be scaled in the range from zero to one, which is the traditional range of a scalar damage parameter d (e.g. Kachanov, 1986):

$$d = e\chi \frac{\ln\left(1 + E_1^0 \mu\right)}{\left(1 + E_1^0 \mu\right)^{\chi}} \quad (0 \leqslant d \leqslant 1) \tag{18}$$

where $\chi (\chi \leqslant 1)$ is the ratio of the strain at maximum tensile stress to the strain at failure and $d = 1$ corresponds to reaching the failure strain. It should be also noted that damage is irreversible and μ (and d) do not decrease if the applied load decreases.

The rate of change of the damage surface is:

$$\dot{\Phi}_1 = \mathbf{s}_1 : \dot{\boldsymbol{\sigma}}_1 - t_1\left(\frac{\partial t_1}{\partial T}\dot{T} + \frac{\partial t_1}{\partial \mu_1}\dot{\mu}_1\right) = 0 \tag{19}$$

The loading/unloading condition can be written as $\dot{\mu} \geqslant 0$, $\Phi_1 \leqslant 0$, $\dot{\mu}\Phi_1 = 0$.

Substituting Eq. (12) in Eq. (4) and pre-multiplying it by $\mathbf{D}_1 = \mathbf{C}_1^{-1}$ gives

$$\dot{\boldsymbol{\sigma}}_1 = \mathbf{D}_1 : \dot{\boldsymbol{\varepsilon}}_1^* - \dot{\mu}_1 \mathbf{D}_1 : \mathbf{s}_1 \tag{20}$$

where

$$\dot{\boldsymbol{\varepsilon}}_1^* = \dot{\boldsymbol{\varepsilon}}_1 - \left(T \frac{\partial \mathbf{C}_1}{\partial T} : \boldsymbol{\sigma}_1 + \dot{\boldsymbol{\varepsilon}}_{\text{th}} \right) \tag{21}$$

From Eq. (19)–(21) the damage rate is

$$\dot{\mu}_1 = \frac{\mathbf{s}_1 : \mathbf{D}_1 : \dot{\boldsymbol{\varepsilon}}_1^*}{\mathbf{s}_1 : \mathbf{D}_1 : \mathbf{s}_1 + t_1 \frac{\partial t_1}{\partial \mu_1}} + \dot{\mu}_{1,\text{th}} \tag{22}$$

where $\dot{\mu}_{1,\text{th}}$ is the extra thermal damage

$$\dot{\mu}_{1,\text{th}} = \frac{-t_1 \frac{\partial t_1}{\partial T} \dot{T}}{\mathbf{s}_1 : \mathbf{D}_1 : \mathbf{s}_1 + t_1 \frac{\partial t_1}{\partial \mu_1}} \tag{23}$$

The stress rate is

$$\dot{\boldsymbol{\sigma}}_1 = \mathbf{D}_1^{(T)} : \dot{\boldsymbol{\varepsilon}}_1^* - \dot{\mu}_{1,\text{th}} \mathbf{D}_1 : \mathbf{s}_1 \tag{24}$$

where the tangent stiffness matrix is

$$\mathbf{D}_1^{(T)} = \left[\mathbf{D}_1 - \frac{(\mathbf{D}_1 : \mathbf{s}_1) \otimes (\mathbf{D}_1 : \mathbf{s}_1)}{\mathbf{s}_1 : \mathbf{D}_1 : \mathbf{s}_1 + t_1 \frac{\partial t_1}{\partial \mu_1}} \right] \tag{25}$$

2.2. Aggregate material model

A non-associated Drucker–Prager material model and its implicit incremental form is used (Mahnken et al., 2000). It is characterized by a yield function Φ_2 and a plastic potential Φ_2^*.

$$\Phi_2 = \alpha_k I_1^{\sigma_2} + \|\mathbf{s}_2\| - s_y \tag{26}$$

$$\Phi_2^* = \alpha_m I_1^{\sigma_2} + \|\mathbf{s}_2\| \tag{27}$$

where $I_1^{\sigma_2}$ is the first invariant of the stress tensor $\boldsymbol{\sigma}_2$, $\|\mathbf{s}_2\|$ is the norm of the deviatoric part of $\boldsymbol{\sigma}_2$, s_y is the yield stress, α_k and α_m are coefficients, which depend on the angle of internal friction ϕ and the dilatation angle ψ, respectively:

$$\alpha_k = 6 \sin \phi / (3 - \sin \phi) \quad \alpha_m = 6 \sin \psi / (3 - \sin \psi) \tag{28}$$

Since $\boldsymbol{\sigma}_2$ represents the contact stress between aggregate particles and surrounding mortar, the aggregate material model should be understood as a model describing the equivalent material behaviour of the aggregate and its interface with the mortar. So the material data required in Eqs. (26)–(28) may differ from the data obtained by experiments on the aggregate alone.

2.3. Calibration of the model

The mixture rule, Eqs. (1)–(3), which represent the parallel (Voigt) model, overestimates the contribution of the aggregate and gives the upper bound of the stiffness of concrete. The lower bound is given by the serial (Reuss) model, which is in better agreement with experimental data. The latter, however, is not suitable for FEM analysis, because it assumes equal stresses and different strains, hence displacements, for the mortar and aggregate. The parallel model can give the same modulus of elasticity as the serial one if an equivalent aggregate modulus is computed from:

$$E_2 = \frac{\alpha_1(r-1)+r}{\alpha_1(r-1)+1}E_1 \tag{29}$$

where $r = \bar{E}_2/E_1$ and $\bar{E}_2$ is the original elasticity modulus for the aggregate. It is assumed that $r = 3$, which corresponds to the experimental data given by Cho et al. (2000).

Constant values are used for the following material data: Poisson ratio $\nu_1 = \nu_2 = 0.2$; plastic coefficient $\lambda = 0$; tensile/compressive strength ratio $\sqrt{c} = f_t/f_c = 0.1$. The volume fractions are taken to be $\alpha_1 = \alpha_2 = 0.5$. All other material parameters are varied independently and used in finite element analyses of a cube in uniaxial and biaxial compression ($\sigma_x/\sigma_y = 1/1$ and $\sigma_x/\sigma_y = 1/0.4$) at various temperatures ($T = 20$, 300, 450 and 600 °C, with $\dot{T} = 0$), according to the experiments performed by Ehm and Schneider (1985). For a given temperature a set of material properties is selected to best fit the experimental results for all loading cases. Since derivatives with respect to temperature are required for the Young's modulus and strength of mortar the discrete values are interpolated by continuous functions (plotted also in Fig. 1):

$$E_1 = \frac{32.3}{1+\exp(0.0068T-1.5)^{1.13}} \quad [\text{GPa}] \tag{30}$$

$$f_t = 6.5 - 14\exp(-430T^{-0.9}); \quad s_y = 2f_t \quad [\text{MPa}] \tag{31}$$

$$\phi = \begin{cases} 18 & \text{if } T \leqslant 100\ ^\circ\text{C} \\ 18 - \frac{T-100}{500} & \text{if } T > 100\ ^\circ\text{C}; \quad \psi = \frac{2}{3}\phi \quad [\text{deg}] \end{cases} \tag{32}$$

The finite element results, using the material properties defined above, are shown together with the experimental data of Ehm and Schneider (1985) in Fig. 2. Solid 3D and 2D plane strain elements give practically identical results. The agreement with the experimental data is good. Further calibration may be achieved by using a temperature dependence for the Poisson ratios ν_1 and ν_2, and the plastic coefficient λ. The corresponding damage evolution is presented in Fig. 3.

The transverse splitting stress σ_y in the mortar, when concrete is under uniaxial compressive stress σ_x, is presented in Fig. 4. The sudden increase in σ_y corresponds to the initiation and growth of the cracks parallel to the direction of loading x. The existence of such cracks is a well known fact (Wastiels, 1979, and the reference contained therein) and they cannot be predicted by the classical theories of plasticity and fracture mechanics. A similar situation arises when the axial compressive stress is due to restrained thermal dilatation. The observed failure is spalling, i.e. brittle failure with most fracture planes parallel to the heated surface (Ulm et al., 1999; Bažant, 1997).

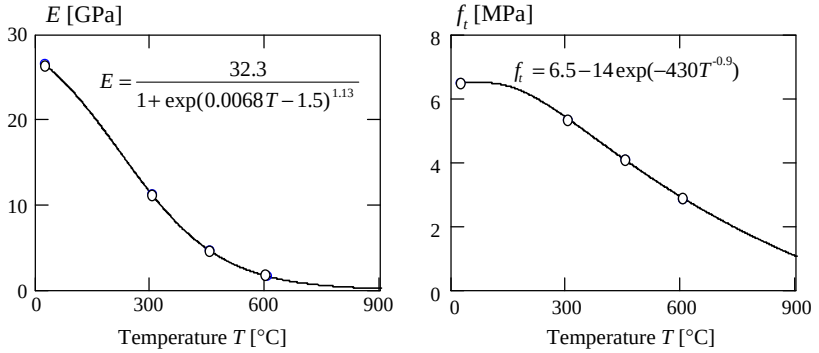

Fig. 1. Elastic modulus E_1 [GPa] and tensile strength f_t [MPa] of mortar. Continuous interpolation of the discrete data 'o' which best fits the experimental graphs of Ehm and Schneider (1985).

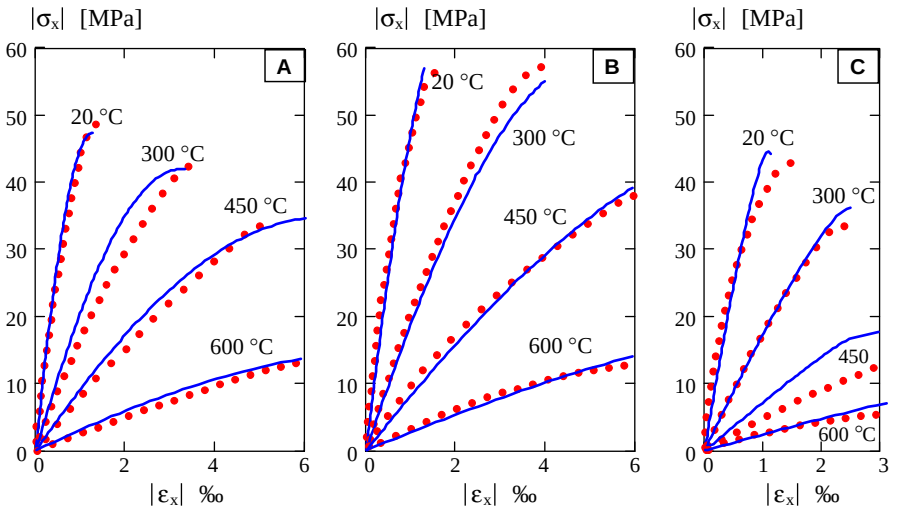

Fig. 2. Stress as function of strain for a cube in uniaxial or biaxial compression at various temperatures and load ratios. Solid lines—3D FEM results; dot lines—experimental data(Ehm and Schneider, 1985). Graphs A: $\sigma_x/\sigma_y = -1/-1$; Graphs B: $\sigma_x/\sigma_y = -1/-0.4$; Graphs C: $\sigma_x/\sigma_y = -1/0$.

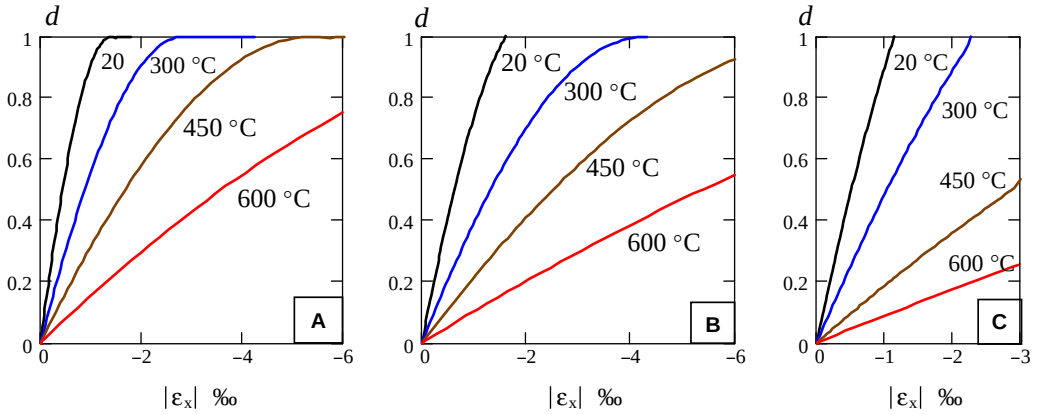

Fig. 3. Damage parameter d as function of strain for a cube in uniaxial or biaxial compression at various temperatures and load ratios. Graphs A: $\sigma_x/\sigma_y = -1/-1$; Graphs B: $\sigma_x/\sigma_y = -1/-0.4$; Graphs C: $\sigma_x/\sigma_y = -1/0$.

2.4. Transient creep strain

The calibration of the model in Section 3 has been done for a concrete specimen, which has been slowly heated to a state of uniform temperature and is free from thermal stresses. In the case of more rapid heating transient creep strain has been observed and the following stress–strain relationship has been proposed (Schneider, 1986, 1988; Purkiss, 1996):

$$\mathrm{d}\sigma_x = \frac{E_x(T,\varepsilon_x,\sigma_x)}{k(\varepsilon_x) + \Phi(T,\sigma_x,w) + 1}\,\mathrm{d}\varepsilon_x \tag{33}$$

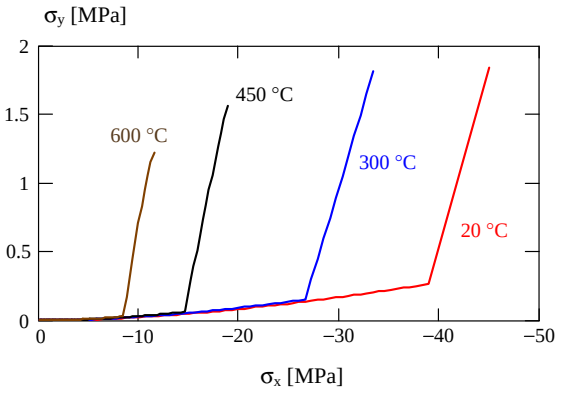

Fig. 4. Splitting stress σ_y in mortar when concrete is under compressive stress σ_x.

where $E_x(T, \varepsilon_x, \sigma_x)$ is the modulus of elasticity depending on temperature, stress and strain, $k(\varepsilon_x)$ is a parameter allowing for non-linear stress–strain behaviour above half the concrete strength (in the present study these effects are assumed to be covered by the damage evolution in the Ortiz model) and $\Phi(T, \sigma_x, w)$ is a transient creep function:

$$\Phi(T, \sigma_x, w) = g(T, \sigma_x)[C_1 \tanh \gamma_w (T - 20) + C_2 \tanh \gamma_0 (T - T_g) + C_3 + 1] - 1 \tag{34}$$

where:

$$g(T, \sigma_x) = 1 + \frac{\sigma_x(T)}{f_{c,20^\circ}} \left(\frac{T - 20}{100} \right); \quad \gamma_w = 0.001 \times (0.3w + 2.2) \tag{34a}$$

and w is the relative water content computed from the hygro-thermal analysis. The coefficients (Purkiss, 1996) are: $C_1 = 2.6$; $C_2 = 2.4$; $C_3 = 2.4$; $\gamma_0 = 0.0075$; $T_g = 650$ °C.

The mismatch in the thermal deformations of aggregate and mortar is believed to be the major reason for the transient creep strain. On a macro level this means that not all of the free thermal strain ε^0_{th}, a cubic polynomial of T (Purkiss, 1996), is 'converted' to mechanical, stress-producing strain when the thermal deformation is constrained. To account for this a modified thermal strain is used in the present study:

$$\varepsilon_{th,i} = \frac{\varepsilon^0_{th}}{\Phi(T, \sigma_i, w) + 1} \quad (i = x, y, z) \tag{35}$$

An alternative approach to account for the thermal transient creep is proposed by Anderberg and Thelandersson (1976) and extended to 3D by Nechnech et al. (2002). Its rate is assumed to be proportional to the rate of temperature, the thermal expansion coefficient and the ratio of the applied stress to the concrete strength at room temperature, $f_{c,20^\circ}$. The latter can be computed from the tensile strength of concrete at room temperature, $f_{t,20^\circ}$, and the ratio used in Ortiz model $f_{t,20^\circ}/f_{c,20^\circ} = \sqrt{c} = 0.1$. The tensile strength of concrete $f_{t,20^\circ}$ is computed from the tensile strengths of mortar and aggregate, Eq. (31), the mixture rule, Eq. (2), and the assumption of equal volume fractions $\alpha_1 = \alpha_2 = 0.5$.

The effect of the thermal transient creep on the axial thermal stress in a column with built-in ends, when the temperature changes uniformly in its volume, can be seen in Fig. 5. For the temperature range 150–200 °C the two models give similar results. It is the opinion of Purkiss (1996) that Schneider's transient creep function gives more realistic stress prediction at high temperatures (400–600 °C) and hence this function is used in Eq. (35).

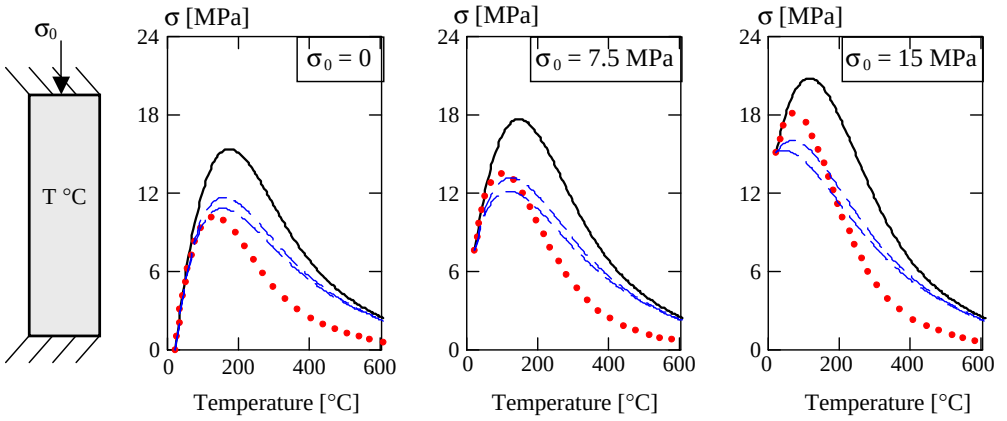

Fig. 5. Thermal stress in a built-in column with axial pre-stress σ_0. Temperature is spatially uniform. Solid line—thermal transient creep neglected. Dot line—thermal transient creep function according to Schneider, Eq. (35). Dash lines—thermal transient creep $\dot{\varepsilon}^{\mathrm{tm}} = \alpha\beta_0\dot{T}(\sigma/f_{c,20^\circ})$ (Anderberg and Thelandersson, 1976), using the two limiting values for β_0: $\beta_0 = 1.8$ and $\beta_0 = 2.35$.

2.5. Thermodynamics considerations

Stabler and Baker (2000) and Stabler (2000) have shown that in coupled thermo-mechanical problems with isotropic damage and an assumption of a constant specific heat, the mechanical dissipation is negative and the second law of thermodynamics is violated. They use the following form for the free energy, which is applicable to transient elevated temperatures:

$$\psi = \frac{1}{2}\boldsymbol{\varepsilon} : \mathbf{E}(g,d) : \boldsymbol{\varepsilon} - \vartheta\mathbf{m}(g,d) : \boldsymbol{\varepsilon} + c(g,d)\left[\vartheta - \theta\ln\left(\frac{\theta}{\theta_0}\right)\right] \tag{36}$$

where g and d are the thermal and mechanical damage coefficients; $\vartheta = \theta - \theta_0$ is the temperature increase; θ is the temperature in [K]; c is the specific heat capacity [J/(m^3 K)]; $\mathbf{m}$ is thermo-elastic coupling tensor—$\vartheta\mathbf{m} = \mathbf{E}$: $\boldsymbol{\varepsilon}_{\mathrm{th}}$, where $\boldsymbol{\varepsilon}_{\mathrm{th}} = \beta\vartheta\mathbf{1}$ is the thermal strain tensor and β is the coefficient of thermal expansion. The mechanical dissipation is:

$$\phi_{\mathrm{mech}} = -\left(\frac{\partial\psi}{\partial d}\dot{d} + \frac{\partial\psi}{\partial g}\dot{g}\right) \tag{37}$$

Following the work of Stabler and Baker (2000) the mechanical dissipation for an approximation of the presented material model has been computed. The approximation involves the definition of a thermal damage as a linear function of temperature. The thermal damage thus defined is used for a linear approximation of the Young modulus, Eq. (30), and the specific heat capacity ρC (ρ is assumed constant and the specific heat C is quadratic polynomial of the temperature, as given in Eurocode EN 1992-1-2). When computing the mechanical damage derivative $\partial\varphi/\partial d$ the elasticity tensor of the mortar, computed from the 1D stress–strain relationship, Eqs. (14)–(16) and Eq. (31), is used. Computations have been made with a constant and with temperature dependant thermal expansion coefficient, with and without using the transient creep function in Eq. (35). In all cases positive mechanical dissipation has been computed.

3. Hygro-thermal analysis

The coupled system of differential equations for heat and mass transfer in a porous material is derived from the following basic laws for energy and mass conservation:

Energy conservation:

$$\underbrace{(\underline{\rho C})\frac{\partial T}{\partial t}}_{a} = \underbrace{\nabla\cdot(k_{\text{eff}}\nabla T)}_{b} - \underbrace{(\underline{\rho C}\mathbf{v})\cdot\nabla T}_{\text{c}} - \underbrace{\lambda_{\text{E}}\dot{E}_{\text{L}}}_{d} - \underbrace{\lambda_{DE}\frac{\bar{\rho}_{\text{D}}}{\partial t}}_{e} \tag{38}$$

Term '*a*' represents the rate of change of the accumulated energy in a unit volume (T—temperature; t—time; $\underline{\rho C}$—effective heat capacity of concrete when it is considered a mixture of dry skeleton, water and gas). Term '*b*' represents the energy diffused by conduction (k_{eff}—the effective thermal conductivity). Term '*c*' represents the energy transferred by fluid flow, i.e. convection. Term '*d*' represents energy required for evaporation of liquid water (λ_{E}—latent heat of evaporation, $\dot{E}_{\text{L}}$—rate of evaporation). Term '*e*' represents the combined energy required for release of bound water by dehydration and eventually its evaporation if the thermodynamic conditions are such that water in a liquid state cannot exist ($\bar{\rho}_{\text{D}}$—density of bound water per unit volume of concrete; $\lambda_{\text{DE}} = \lambda_{\text{D}} + \lambda_{\text{E}}(1-\Theta)$; λ_{D}—specific heat of dehydration of bound water; $\Theta = 1$ when $P_{\text{G}}/P_{\text{Sat}} \geqslant 1$, i.e. bound water is released as liquid water or $\Theta = 0$ when $P_{\text{G}}/P_{\text{Sat}} < 1$, i.e. bound water is released as water vapour).

Liquid water conservation:

$$\underbrace{\frac{\partial\bar{\rho}_{\text{L}}}{\partial t}}_{a} = \underbrace{-\nabla\cdot\mathbf{J}_{\text{L}}}_{b}\ \underbrace{-\dot{E}_{\text{L}}}_{\text{c}} + \underbrace{\Theta\frac{\partial\bar{\rho}_{\text{D}}}{\partial t}}_{d} \tag{39}$$

Term '*a*' represents the rate of change of liquid water content $\bar{\rho}_{\text{L}}$ in a unit volume of concrete, term '*b*'—the mass of water transferred by convection, term '*c*'—mass lost by evaporation, term '*d*'—mass gained from dehydration of chemically bound water.

Water vapour conservation:

$$\frac{\partial(\varepsilon_{\text{G}}\tilde{\rho}_{\text{V}})}{\partial t} = -\nabla\cdot\mathbf{J}_{\text{V}} + \dot{E}_{\text{L}} + (1-\Theta)\frac{\partial\bar{\rho}_{\text{D}}}{\partial t} \tag{40}$$

Air conservation:

$$\frac{\partial(\varepsilon_{\text{G}}\tilde{\rho}_{\text{A}})}{\partial t} = -\nabla\cdot\mathbf{J}_{\text{A}} \tag{41}$$

The mass fluxes are:

$$\mathbf{J}_{\text{A}} = \varepsilon_{\text{G}}\tilde{\rho}_{\text{A}}\mathbf{v}_{\text{G}} - \varepsilon_{\text{G}}\tilde{\rho}_{\text{G}}D_{\text{AV}}\nabla(\tilde{\rho}_{\text{A}}/\tilde{\rho}_{\text{G}}) \tag{42}$$

$$\mathbf{J}_{\text{V}} = \varepsilon_{\text{G}}\tilde{\rho}_{\text{V}}\mathbf{v}_{\text{G}} - \varepsilon_{\text{G}}\tilde{\rho}_{\text{G}}D_{\text{AV}}\nabla(\tilde{\rho}_{\text{A}}/\tilde{\rho}_{\text{G}}) \tag{43}$$

$$\mathbf{J}_{\text{L}} = \bar{\rho}_{\text{L}}\mathbf{v}_{\text{L}} \tag{44}$$

The velocities of the gaseous mixture and liquid water are assumed to be related to the corresponding pore pressure gradients via Darcy's law:

$$\mathbf{v}_{\text{G}} = -\frac{KK_{\text{G}}}{\mu_{\text{G}}}\nabla P_{\text{G}} \quad \mathbf{v}_{\text{L}} = -\frac{KK_{\text{L}}}{\mu_{\text{L}}}\nabla P_{\text{L}} \tag{45}$$

The following notations are used: ε_{G}—volume fraction of the gaseous mixture, D_{AV}—diffusion coefficient between dry air and water vapour; K—concrete permeability, $\tilde{\rho}_i$—density of phase i per unit volume of gaseous mixture, P_i—pressure, $\mathbf{v}_i$—velocity, K_i—relative permeability, μ_i—dynamic viscosity. Phase subscript i: A—dry air; G—gaseous mixture; L—liquid water phase; V—water vapor. No distinction is made between free liquid water in the pores and adsorbed water on the pore surface. The liquid water flux $\mathbf{J}_{\text{L}}$ may be regarded as the average of these fluxes.

Air and water vapour are assumed to obey the ideal gas law. The equilibrium between water vapour and liquid water content is assumed to be governed by the sorption curves (Bažant and Thonguthai, 1978).

After eliminating the rate of evaporation in Eq. (38)–(41) a system of three differential equations remains which is solved for T, P_G, and $\tilde{\rho}_V$. A full description of the model and its finite element discretisation is given by Tenchev et al. (2001a) and some variations in Tenchev et al. (2001b), Tenchev et al. (2001c), Li et al. (2002).

3.1. Coupling pore pressure and damage

To take into account the influence of pore pressure on the evolution of damage the strain, as well as the stress increments associated with it, has to be computed and used in the presented material model. This can be done if the pore pressure is applied as a body force in the FEM stress analysis. The magnitude of the body force $\boldsymbol{F}$ can be computed from the pore pressure gradients:

$$F_x = b\frac{\partial P_G}{\partial x}; \quad F_y = b\frac{\partial P_G}{\partial y}; \quad F_z = b\frac{\partial P_G}{\partial z} \tag{46}$$

where b ($0 < b \leqslant 1$) is the Biot coefficient (Biot, 1941; Biot, 1956).

The dry skeleton of concrete can be considered incompressible (when compared to the compressibility of the gaseous mixture that causes the pore pressure) thus it can be assumed $b = 1$, (Coussy, 1995). Majumdar et al. (1995) and Majumdar and Marchertas (1997) incorporate the pore pressure in a FEM stress analysis by applying work equivalent surface loads on the element sides. Their approach implies $b = 1$ as well. Ichikawa and England (2004) use a hollow spherical model for the concrete skeleton and derive a 'hydrostatic' tensile stress σ_t as a function of the pore volume, V_P, which for $V_P = 0.16$ gives $\sigma_t = 0.78P_G$.

4. Numerical example

A concrete wall, shown in Fig. 6 (fully fixed top and bottom sections, no initial stress), is exposed on both sides to external temperature following the standard fire curve (Purkiss, 1996). The major hygro-thermal material properties used are: permeability $K = 2 \times 10^{-16}$ m^2; porosity—0.16; initial pore saturation with liquid water—50% (i.e. $\bar{\rho}_L = 80$ [kg/m^3]). The rest of the properties are given in Tenchev et al. (2001a). The results from a 2D coupled thermo–hygro-mechanical finite element analysis are shown in Figs. 7 and 8.

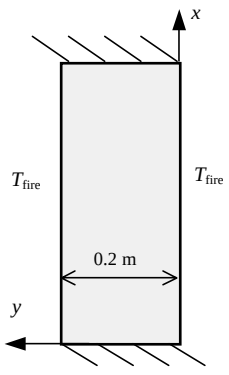

Fig. 6. Layout of the test problem.

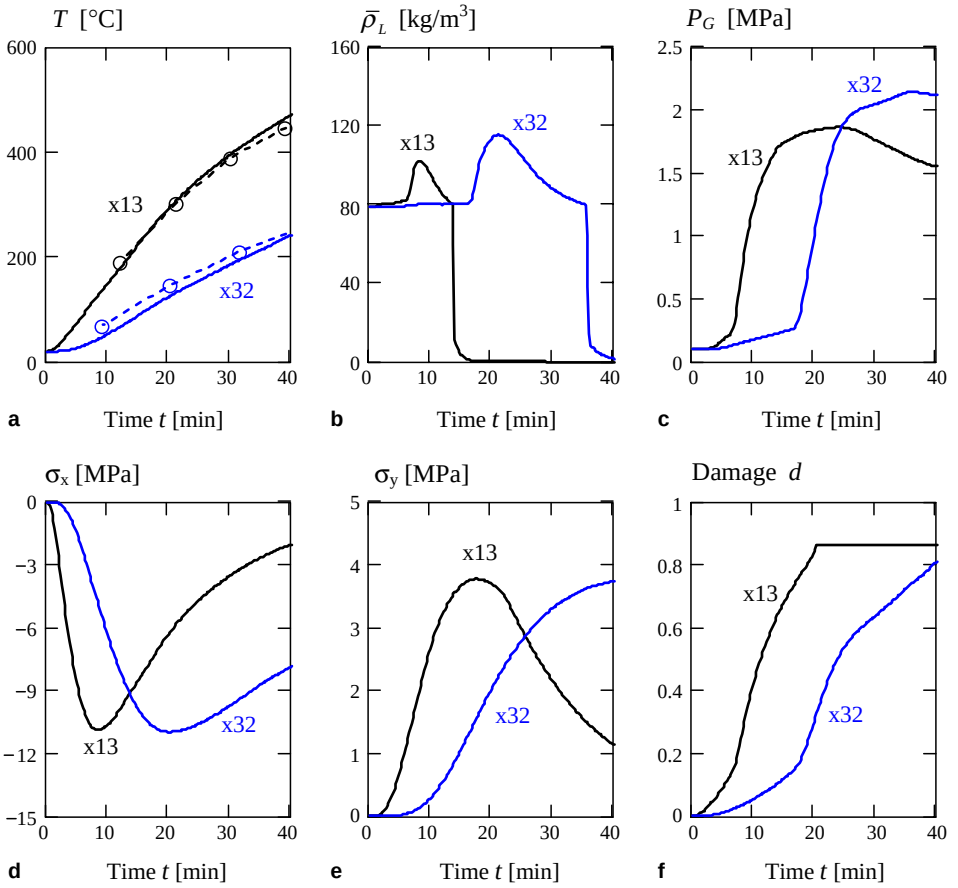

Fig. 7. Computed temperature T, liquid water content per unit volume of concrete $\bar{\rho}_L$, pore pressure P_G, axial stress σ_x, transverse stress σ_y, and damage d at distances $x13 = 0.013$ m and $x32 = 0.032$ m from the fire exposed surface. Lines --o-- in (a)—experimental results by Ahmed and Hurst (1997).

The temperature distributions T [°C] (Fig. 7a and 8a) are in good agreement with the experimental results by Ahmed and Hurst (1997) and El-Dieb and Hooton (1995), shown by the circles on the dashed lines.

The time history of the liquid water content $\bar{\rho}_L$ [kg/m^3], at two locations $x = 0.013$ and 0.032 m, is shown in Fig. 7b. Initially $\bar{\rho}_L$ stays constant until water vapour is transferred from the regions closer to the fire exposed surface where the liquid water has already evaporated. Since the temperature here is lower the vapour condenses, increases the water content and a moisture clog is formed (Harmathy, 1965; Ulm et al., 1999). With the increase of temperature there is a gradual decrease of the liquid water content due to evaporation and mass transfer driven by the pressure gradient. When the temperature reaches its saturation value corresponding to the pore pressure at the given location a rapid evaporation takes place and all liquid water is transformed into vapour.

All of the phenomena described above can been seen in Fig. 8b, where the spatial distribution of the water content at two times, $t = 10$ and 30 min, is presented. Near the fire exposed surface the liquid water content is zero because the temperature is too high and water can exist only as vapour. Towards the interior of the concrete the evaporation front and the 'moisture clog' can be clearly identified.

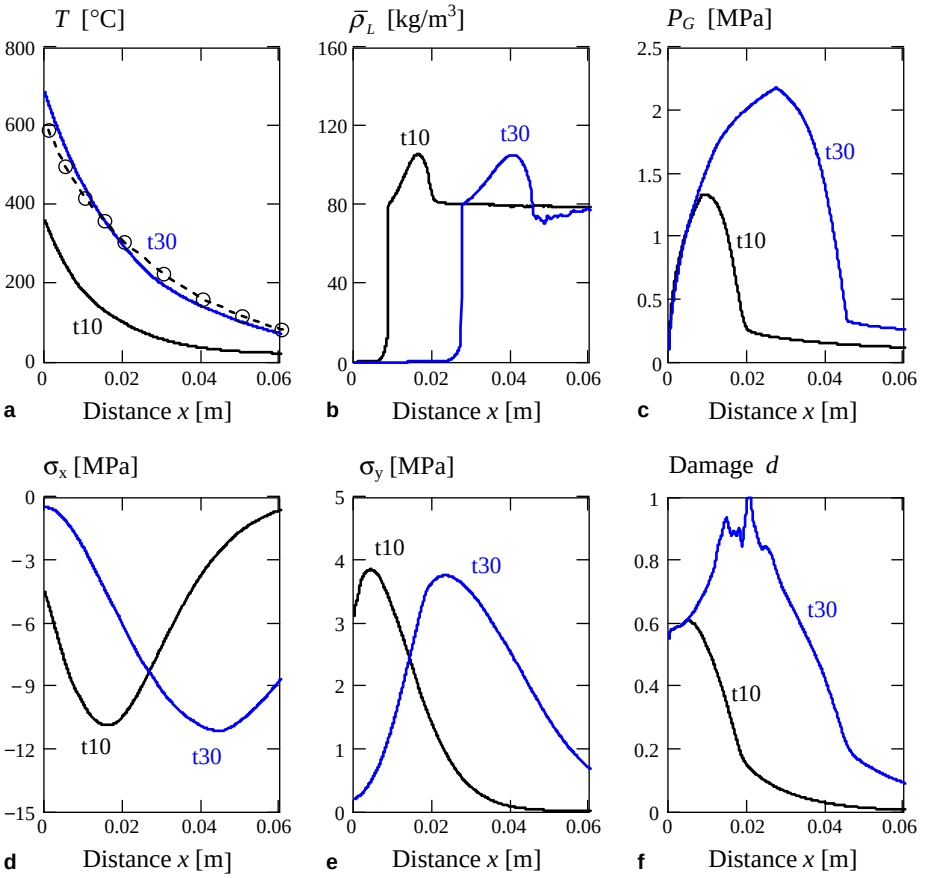

Fig. 8. Computed temperature T, liquid water content per unit volume of concrete $\bar{\rho}_L$, pore pressure P_G, axial stress σ_x, transverse stress σ_y, and damage d at times $t10 = 10$ min and $t30 = 30$ min from the start of fire. Lines --o-- in (a)—experimental results by El-Dieb and Hooton (1995).

The pore pressure distributions P_G [MPa] at the already discussed locations and times are presented in Fig. 7c and 8c, respectively. Pore pressure develops because the rate of evaporation is higher than the rate of vapour transfer. The maximum value of P_G occurs at the evaporation front, where the rate of evaporation is highest. It is in good agreement with the experimental results by Consolazio et al. (1998) and Kalifa et al. (2000).

The axial stress σ_x is shown in Fig. 7d and 8d. It is due to the constrained axial thermal expansion. The transverse stress σ_y is shown in Fig. 7e and 8e. It is the result of mortar/aggregate interaction in Ortiz's model and the thermal stress due to the temperature gradient. The increase of temperature has two competing effects on the magnitude of the stresses: on one hand the stresses increase because the restrained thermal dilatation increases; on the other hand the stresses decrease because the modulus of elasticity decreases. The latter has the dominant effect at high temperatures and the stresses are lower near the fire exposed surface. The maximum values of σ_x and σ_y remain almost constant and shift with time towards the interior. This 'stress wave' causes damage which, being irreversible, remains constant at its maximum value when stresses decrease. The distribution of the damage d is shown in Figs. 7e and 8e. It is mostly due to the transverse tensile stress σ_y.

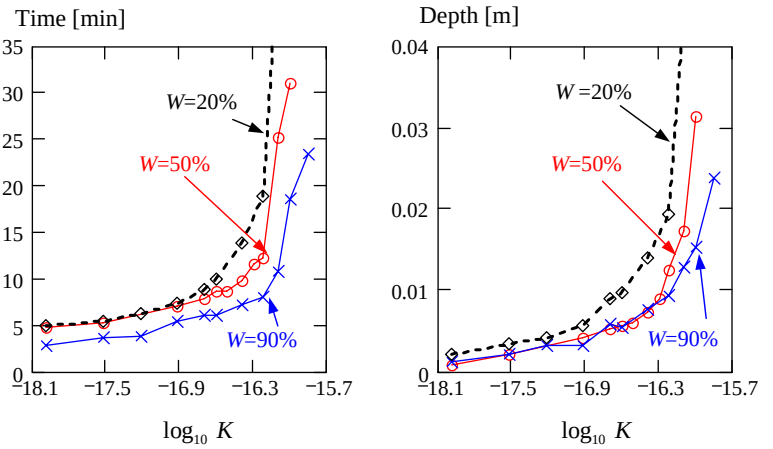

Fig. 9. Time and depth of spalling as function of permeability K [m^2] for three levels of initial free water content $\bar{\rho}_L$.

The presented stresses and damage graphs are computed without applying the pore pressure gradient as a body force, Eq. (46), in the stress analysis module. When it is applied, the result is the algebraic sum of the pore pressure and the stress. The corresponding damage is higher and when it reaches unity a spalling failure can be numerically predicted.

The time and depth of the predicted spalling failure are shown in Fig. 9. The results are presented for a practical range of variation of permeability K (England and Khoylou, 1995). Several levels of initial free water content are considered. They are defined by the percentage of the pore space filled with water. Thus $W = 50\%$ stands for initial water content of $\bar{\rho}_L = 80$ kg/m^3 (since porosity is 0.16 and water density is 1000 kg/m^3) which is the value used in the analyses presented in Figs. 7 and 8. Graph termination to the right, where K increases, means than no spalling has been predicted during the first 60 min of fire exposure simulation. The high gradient also points to the existence of a threshold value of K beyond which spalling will not occur. The computed results follow the general tendencies observed experimentally (Purkiss, 1996)—spalling is more likely to happen in high strength concrete, whose permeability corresponds to the lower values of K in Fig. 9, and in concrete with higher initial water content. The numerical results are in good agreement with published experimental data. Ali et al. (2001) have reported spalling of high-strength concrete to occur after 5–22 min of fire exposure, Aldea et al. (1997)—after 8 min. Anderberg (1997) has reported that the depth of spalling for high performance concrete was about 5–10 mm, while for ordinary concrete—about 20–40 mm.

The influence of the axial pre-load on spalling will be investigated in future studies. It has two opposing effects—on one hand the axial pre-load increases the axial and transverse stresses, on the other hand it causes microcracking, which reduces the magnitude of the pore pressure. The contradicting effects of the two competing mechanisms can be found in the published experimental data. Sullivan (2004) has reported that the axial pre-load decreases the chance of explosive spalling, Connolly (1997) and Anderberg (1997)—that it increases it, and Ali et al. (2001)—that it has no effect. For correct modeling of the latter a coupling between the level of stress (or damage) and concrete permeability and porosity has to be established, similarly to Gawin et al. (2002).

5. Conclusions

A material damage model, proposed by Ortiz (1985), has been extended to account for the effects of high temperature. The temperature dependence of some of the material properties has been calibrated with

published experimental results for uniaxial and biaxial loading at high temperature, (Ehm and Schneider, 1985) and it has been possible to achieve a good agreement between the numerical and the experimental results.

The model has been included in a coupled thermo–hygro-mechanical finite element analysis. The failure mechanism of concrete exposed to high temperature, as in the case of fire, is thermal spalling. The evolution of the damage variable in Ortiz's model has been used for its prediction.

A transient creep functions proposed by Schneider (1986) has been used in the computation of the thermal stresses to account for the transient creep strain.

The effect of pore pressure on the damage evolution has been modeled by applying a body force in the stress analysis module proportional to the pressure gradient.

The numerical example solved has shown good agreement with published experimental data for the temperature and pore pressure distributions as well as for the time and depth of the predicted spalling.

Acknowledgement

The authors acknowledge the financial support by EPSRC, grant no. GR/R09244/01.

References

Ahmed, G.N., Hurst, J.P., 1997. An analytical approach for investigating the cases of spalling of high-strength concrete at elevated temperatures. In: International Workshop on Fire Performance of High-Strength Concrete. NIST Gaithersburg, MD, February 13–14, Paper B.6, pp. 95–108.

Aldea, C.M., Franssen, J.M., Dotreppe, J.C., 1997. Fire test on normal and high-strength reinforced concrete columns. In: International Workshop on Fire Performance of High-Strength Concrete. NIST Gaithersburg, MD, February 13-14, Paper B7, pp. 109–124.

Ali, F.A., O'Connor, D., Abu-Tair, A., 2001. Explosive spalling of high-strength concrete columns in fire. Mag. Concr. Res. 53, 197–204.

Anderberg, Y., 1997. Spalling phenomena of HPC and OC. In: Phan, L.T., Carino, N.J., Duthinh, D., Garboczi, E. (Eds.), Proceedings of International Workshop on Fire Performance of High-Strength Concrete, NIST Spec. Publ. 919. National Institute of Standards and Technology, Gaithersburg, MD, pp. 69–74.

Anderberg, Y., Thelandersson, S., 1976. Stress and deformation characteristics of concrete at high temperature. Bulletin 54, Lund Institute of Technology, Lund.

Baggio, P., Majorana, C.E., Schrefler, B.A., 1995. Thermo-hygro-mechanical analysis of concrete. Int. J. Num. Meth. Fluids 20, 573–595.

Bažant, Z.P., Thonguthai, W., 1978. Pore pressure and drying of concrete at high temperature. J. Eng. Mech. Div. ASCE 104, 1059–1079.

Bažant, Z.P., 1997. Analysis of pore pressure thermal stresses and fracture in rapidly heated concrete. In: Phan, L.T., Carino, N.J., Duthinh, D., Garboczi, E. (Eds.), Proceedings of International Workshop on Fire Performance of High-Strength Concrete, NIST Spec. Publ. 919. National Institute of Standards and Technology, Gaithersburg, MD, pp. 155–164.

Biot, M.A., 1941. General theory of three-dimensional consolidation. J. Appl. Phys. 12 (1), 155–164.

Biot, M.A., 1956. General solutions of the equations of elasticity and consolidation for a porous material. J. Appl. Mech. 23, 91–96.

Carol, I., Rizzi, E., William, K., 1994. A unified theory of elastic degradation and damage based on a loading surface. Int. J. Solids Struct. 31 (20), 2835–2865.

Cho, S.W., Yang, C.C., Huang, R., 2000. Effect of aggregate volume fraction on the elastic moduli and void ratio of cement-based materials. J. Mar. Sci. Technol. 8 (1), 1–7.

Connolly, R., 1997. The spalling of concrete. Fire Eng. J. (January), 38–40.

Consolazio, G.R., McVay, M.C., Rish III., J.W., 1998. Measurement and prediction of pore pressures in saturated cement mortar subjected to radiant heating. ACI Mater. J. 95 (5), 526–536.

Coussy, O., 1995. Mechanics of Porous Continua. John Wiley & Sons.

Ehm, C., Schneider, U., 1985. The high temperature behaviour of concrete under biaxial conditions. Cement Concr. Res. 15, 27–34.

El-Dieb, A.S., Hooton, R.D., 1995. Water-permeability measurement of high performance concrete using a high-pressure triaxial cell. Cement Concr. Res. 25, 1199–1208.

England, G.L., Khoylou, N., 1995. Moisture flow in concrete under steady state non-uniform temperature states: experimental observations and theoretical modelling. Nucl. Eng. Des. 156, 83–107.

Faria, R., Oliver, J., Cervera, M., 1998. A strain-based plastic viscous damage model for massive concrete structures. Int. J. Solids Struct. 35 (14), 1533–1558.

Gawin, D., Majorana, C.E., Schrefler, B.A., 1999. Numerical analysis of hygro-thermal behavior and damage of concrete at high temperature. Mech. Cohes.-Frict. Mater. 4, 37–74.

Gawin, D., Pesavento, F., Schrefler, B.A., 2002. Simulation of damage-permeability coupling in hygro-thermo-mechanical analysis of concrete at high temperature. Commun. Num. Meth. Eng. 18, 113–119.

Harmathy, T.Z., 1965. Effect of moisture on the fire endurance of building materials, ASTM No. 385, Philadelphia, pp. 74–95.

Ichikawa, Y., England, G.L., 2004. Prediction of moisture migration and pore pressure build-up in concrete at high temperatures. Nucl. Eng. Des. 228 (1–3), 245–259.

Kachanov, L.M., 1986. Introduction to Continuum Damage Mechanics. Martinus Nijhoff Publishers, The Netherlands.

Kalifa, P., Menneteau, F-D., Quenard, D., 2000. Spalling and pore pressure in HPC at high temperatures. Cement Concr. Compos. 30, 1915–1927.

Li, L.Y., Purkiss, J.A., Tenchev, R.T., 2002. An engineering model for coupled heat and mass transfer in heated concrete. J. Mech. Eng. Sci. 216, 213–224.

Luccioni, B.M., Figueroa, M.I., Danesi, R.F., 2003. Thermo-mechanic model for concrete exposed to elevated temperatures. Eng. Struct. 25, 729–742.

Mahnken, R., Tikhomirov, D., Stein, E., 2000. Implicit integration scheme and its consistent linearization for an elastoplastic-damage model with application to concrete. Comput. Struct. 75, 135–143.

Majumdar, P., Gupta, A., Marchertas, A., 1995. Moisture propagation and resulting stress in heated concrete walls. Nucl. Eng. Des. 156, 159–165.

Majumdar, P., Marchertas, A., 1997. Heat moisture transport and induced stresses in porous materials under rapid heating. Num. Heat Transfer Part A 32, 111–130.

Nechnech, W., Meftah, F., Reynouard, J.M., 2002. An elasto-plastic damage model for plain concrete subjected to high temperature. Eng. Struct. 24, 597–611.

Ortiz, M., 1985. A constitutive theory for the inelastic behaviour of concrete. Mech. Mater. 4, 67–93.

Papa, E., Taliecio, A., 1996. Anisotropic damage model for the multiaxial static and fatigue behaviour of plain concrete. Eng. Fract. Mech. 55 (2), 163–179.

Purkiss, J.A., 1996. Fire Safety Engineering Design of Structures. Butterworth-Heinemann.

Schneider, U., 1986. Modelling of concrete behaviour at high temperatures. In: Design of Structures Against Fire. Elsevier Applied Science, London, pp. 53–70.

Schneider, U., 1988. Concrete at high temperatures—a general review. Fire Safety J. 13, 55–68.

Simo, J.C., Ju, J.W., 1987. Strain- and stress-based continuum damage models – I Formulation. Int. J. Solids Struct. 23 (7), 821–840.

Smith, G.M., Young, L.E., 1955. Ultimate theory in flexure by exponential functions. In: Proc. ACI 61(2), 195.

Stabler, J., Baker, G., 2000. On the form of free energy and specific heat in coupled thermo-elasticity with isotropic damage. Int. J. Solids Struct. 37, 4691–4713.

Stabler, J., 2000. Computational modelling of thermo-mechanical damage and plasticity in concrete. Ph.D. Thesis, Department of Civil Engineering, The University of Queensland.

Sullivan, P.J.E., 2004. A probabilistic method of testing for the assessment of deterioration and explosive spalling of high strength concrete beams in flexure at high temperature. Cement Concr. Compos. 26, 155–162.

Tenchev, R.T., Li, L.Y., Purkiss, J.A., 2001a. Finite element analysis of coupled heat and moisture transfer in concrete subjected to fire. Num. Heat Transfer, Part A: Appl. 39 (7), 685–710.

Tenchev, R.T., Li, L.Y., Purkiss, J.A., 2001b. Numerical analysis of temperature and pore pressure in intensely heated concrete. In: 9th ACME Conference. University of Birmingham, UK, pp. 5–8.

Tenchev, R.T., Li, L.Y., Purkiss, J.A, Khalafallah, B.H., 2001c. Finite element analysis of coupled heat and mass transfer in concrete when it is in fire. Mag. Concr. Res. 53 (2), 117–125.

Ulm, F.J., Coussy, O., Bažant, Z.P., 1999. The "Chunnel" Fire. I: Chemoplastic softening in rapidly heated concrete. The "Chunnel" Fire. II: Analyses of concrete damage. J. Eng. Mech. ASCE 125 (3), 272–289.

Wastiels, J., 1979. Behavior of concrete under multiaxial stresses—a review. Cement Concr. Res. 9, 35.

Yazdani, S., Schreyer, H.L., 1998. An anisotropic damage model with dilatation for concrete. Mech. Mater. 7, 231–244.